

JGR Atmospheres

RESEARCH ARTICLE

10.1029/2018JD029155

Key Points:

- Assuming the standard atmosphere, ice nucleation is controlled by soot number emissions above 270 hPa and below additionally by temperature
- For current aircraft emissions, around 90% of emitted soot particles form on average ice crystals at extratropical cruise altitudes
- At tropical cruise altitudes 60% of contrails form near the formation threshold and the ice crystal number formed is reduced by around 50%

Correspondence to:

A. Bier,
andreas.bier@dlr.de

Citation:

Bier, A., & Burkhardt, U. (2019). Variability in contrail ice nucleation and its dependence on soot number emissions. *Journal of Geophysical Research: Atmospheres*, 124. <https://doi.org/10.1029/2018JD029155>

Received 14 JUN 2018

Accepted 10 FEB 2019

Accepted article online 16 FEB 2019

Author Contributions:

Supervision: U. Burkhardt

Visualization: A. Bier

Writing - original draft: A. Bier

Writing - review & editing: A. Bier, U. Burkhardt

Variability in Contrail Ice Nucleation and Its Dependence on Soot Number Emissions

A. Bier¹  and U. Burkhardt¹ 
¹Deutsches Zentrum für Luft- und Raumfahrt, Institut für Physik der Atmosphäre, Oberpfaffenhofen, Germany

Abstract Contrail ice nucleation is mainly controlled by aircraft emissions and the atmospheric state. The nucleation rate can have a strong impact on microphysical processes, optical properties, lifetime, and, therefore, on the climate impact of contrail cirrus. We study contrail ice crystal formation offline for specified atmospheric conditions and its spatial variability in a global climate model. Assuming the standard atmosphere, above around 270 hPa (10 km) contrail ice nucleation is mainly controlled by aircraft soot number emissions and below additionally by atmospheric temperature. Parameterizing contrail ice nucleation in a global climate model, we find that in the northern extratropics contrails form frequently far away from their formation threshold. For current soot number emissions and in case of contrail formation, 90% of emitted soot particles form on average ice crystals around the cruise level and more than 70% between cruise altitudes and 300 hPa. The number of nucleated ice crystals in the extratropics decreases nearly at the same rate as soot number emissions. In contrast, in the tropics around cruise altitudes approximately 60% of contrails develop close to their formation threshold so that on average only about 50% of emitted soot particles can form ice crystals. Below, contrail formation occurs rarely and ice nucleation is reduced more strongly. Of the main air traffic areas, contrail ice nucleation is significantly limited by the atmospheric state over eastern Asia and over the southeastern United States. This limitation is enhanced during the summer months.

1. Introduction

Aviation causes around 5% of the anthropogenic global radiative forcing or about 100 mW/m² for the year 2005 (Lee et al., 2009), an estimate based on modeling and observations. The largest known contribution is caused by contrail cirrus (Burkhardt & Kärcher, 2011), consisting of young contrails and aged contrails which have lost their line shape. A slightly smaller contribution is due to accumulated aircraft-emitted carbon dioxide and significantly smaller contributions originate from emitted NO_x, water vapor, and the direct effect of emitted aerosol particles. Using an air traffic inventory for the year 2006, Bock and Burkhardt (2016b) and Schumann et al. (2015) estimate the radiative impact by contrail cirrus to amount around 60 mW/m². The indirect aerosol effect on clouds has not been reliably quantified yet (Boucher et al., 2013). The yearly growth of Revenue Passenger Kilometers by around 5% and aircraft fuel consumption by 6–10% (International Civil Aviation Organization, 2013) implies a continuous increase in the aviation climate impact and its relative contribution to the anthropogenic climate forcing.

Contrails form at sufficiently low ambient temperatures, when water saturation is reached or surpassed within the aircraft plume during isobaric mixing of the hot and moist engine exhaust air with the drier and colder atmospheric air (Schumann, 1996). They persist when air is at least saturated relative to ice. This means that contrails form and persist at ambient relative humidities lower than necessary for natural cirrus cloud formation (Koop et al., 2000). In the water supersaturated plume, aerosol particles activate into water droplets and rapidly freeze into ice crystals by homogeneous nucleation (Kärcher & Yu, 2009). Pressure differences along the wing tips of aircraft lead to a pair of counterrotating vortices (Paoli & Shariff, 2016) in which most of the formed ice crystals are trapped. The adiabatic heating during the descent of these vortices causes a decrease in relative humidity which can lead to the sublimation of ice crystals at ice-subsaturated conditions (Lewellen & Lewellen, 2001; Sussmann & Gierens, 1999). After vortex breakup (several minutes after formation), the contrail evolution in the dispersion phase is controlled by the exchange with the surrounding atmosphere (e.g., Bier et al., 2017; Bock & Burkhardt, 2016a; Schumann & Heymsfield, 2017).

In situ measurements have demonstrated that young contrails are characterized by a high number of particularly small ice crystals (e.g., Petzold et al., 2017; Schröder et al., 2000; Voigt et al., 2010). Single contrails have been observed to persist in ice-supersaturated regions for many hours (Gierens & Vazquez-Navarro, 2018; Haywood et al., 2009; Minnis et al., 1998).

The life cycle of contrail cirrus clusters depends strongly on the synoptic situation (Bier et al., 2017). Contrail cirrus clusters, developing in large-scale and long-lived ice-supersaturated areas, tend to be long-lived and climate relevant. A clear reduction in the number of ice crystals at initialization (contrail age of 7.5 min) in such a synoptic state strongly impacts microphysical process rates and decreases the volume of visible contrail cirrus and their shortwave radiative impact significantly. In other situations a reduction in the initial ice crystal number has little impact on the temporal evolution of contrail cirrus properties and their radiative impact. Since it is the long-lived contrails that mainly contribute to the contrail cirrus climate impact (Burkhardt et al., 2018), reducing the number of nucleated contrail ice crystals in large-scale ice-supersaturated areas is an effective mitigation option causing a decrease in contrail cirrus optical depth and lifetime.

Switching to alternative fuels, such as synthetic Fischer-Tropsch fuels and biofuels, has been shown to reduce the number of emitted soot particles in ground-based measurements (Beyersdorf et al., 2014; Moore et al., 2015; Speth et al., 2015). In addition, flight measurements during the ACCESS-I campaign indicate a reduction of soot number emissions by 50–70% when mixing (50:50) conventional kerosene with a biofuel (Moore et al., 2017). Possibilities to further reduce in-flight soot number emissions and, therefore, the number of formed contrail ice crystals are increasing the amount of biofuels in the fuel blend or switching to lean combustion (Foust et al., 2011).

The number of nucleated contrail ice crystals is not only determined by engine soot number emissions but is also controlled by atmospheric conditions (Kärcher et al., 2015). When the contrail formation threshold is well exceeded, the number of nucleated ice crystals is approximately given by the number of emitted soot particles so that a reduction in the soot particle number causes a similar reduction in the number of formed contrail ice crystals. At temperatures close to the contrail formation threshold, maximum plume supersaturation limits the ice nucleation since only the larger soot or ambient particles entrained into the plume can activate into water droplets (Kärcher et al., 2015). Initial ice crystal number in global climate models has been calculated either from the water vapor available for deposition, assuming a fixed ice crystal size (Chen & Gettelman, 2013), or prescribed using a constant initial value inferred from in situ measurements (Bock & Burkhardt, 2016b) or set equal to engine soot number emissions accounting for different aircraft types (Schumann et al., 2015). The method of Chen and Gettelman (2013) introduces a dependency on the atmospheric state that only remotely relates to the nucleation process within contrails. The latter two methods may lead on average to realistic values at midlatitude cruise levels where most of the measurements have been performed, but may overestimate the number of formed ice crystals when the atmosphere is close to the contrail formation threshold, for example, in the tropics.

In this paper, we include the ice nucleation process of contrails, based on the parameterization of Kärcher et al. (2015), within the contrail cirrus scheme of our global climate model in order to study the variability in ice crystal formation due to atmospheric variability and changes in soot number emissions. Our objective is to analyze where and how frequently ice crystal formation is limited by the atmospheric state and where the use of alternative fuels is most effective in reducing contrail ice nucleation.

In section 2, we give an overview over the parameterization of contrail ice crystal formation (Kärcher et al., 2015) and describe our offline studies and the global climate model and simulations. We analyze within offline studies, in section 3, the sensitivity of the nucleated ice crystal number on atmospheric parameters and on flight altitude. In section 4, we show how frequently contrails form close to their formation threshold and to what degree ice nucleation is limited by the atmospheric conditions depending on latitude, season, and height. We discuss the spatial variability in contrail ice nucleation given by the apparent emission index of ice, fuel consumption, air traffic density, and contrail formation probability. Finally, the influence of an 80% reduction in soot number emissions on the number of nucleated ice crystals is analyzed. Summary and conclusions are given in section 5.

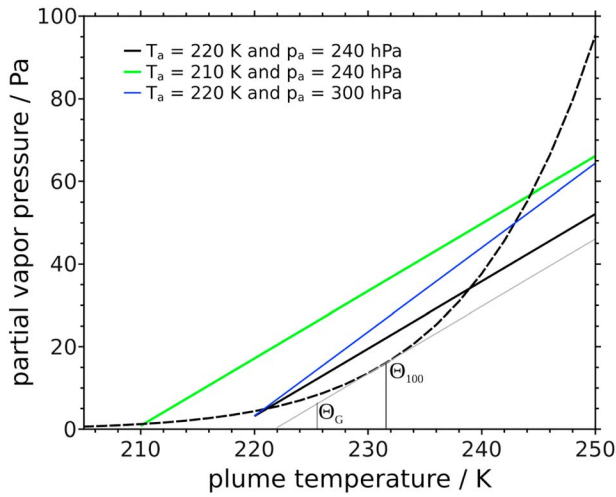


Figure 1. Saturation vapor pressure over water (dashed) and average plume mixing lines indicating the dependency of partial vapor pressure on plume temperature during the mixing of hot exhaust air with colder ambient air for a conventional airliner. The solid, black line characterizes a baseline scenario when the Schmidt-Appleman-criterion is fulfilled with ambient temperature of 220 K and atmospheric pressure of 240 hPa. The green color shows the mixing line when temperature is decreased by 10 K and the blue color when pressure is increased by 60 hPa. The thin gray line indicates a mixing line under threshold conditions at a pressure of 240 hPa; Θ_{100} denotes the threshold temperature in a water-saturated environment and Θ_G the threshold temperature at a relative humidity over water of 76.4% which translates into a relative humidity over ice of 120%.

2. Methods

2.1. Thermodynamic Formation Criterion

Contrails form if the Schmidt-Appleman (SA)-criterion (Schumann, 1996) is fulfilled. Figure 1 illustrates the formation criterion in thermodynamic equilibrium. The mixing lines (solid) characterize isobaric mixing of the hot and moist engine exhaust air with the colder ambient air and approach atmospheric conditions at the end of the mixing. The SA-criterion will be fulfilled if the mixing line crosses the water saturation vapor pressure (dashed) as indicated in Figure 1. In that case water supersaturation within the plume, necessary for droplet formation on plume particles, is generated. The threshold for contrail formation occurs when the mixing line only touches the water saturation vapor pressure (thin line) and is dependent on the slope of the mixing line G . The osculation point (Θ_{100} , Figure 1) characterizes the largest possible temperature for contrail formation in a water-saturated atmosphere and can be approximated according to Schumann (1996) by

$$\Theta_{100} = -46.46 + 9.43 \ln(G-0.053) + 0.720[\ln(G-0.053)]^2, \quad (1)$$

where

$$G = \frac{M_w c_p p_a}{0.622 Q (1-\eta)} \quad (2)$$

is the slope of the mixing line with c_p indicating the specific heat capacity of water, M_w exhaust vapor mass emission index, Q combustion heat, η propulsion efficiency, and p_a atmospheric pressure. Given a fixed slope G , the SA-threshold temperature in a water-subsaturated environment

(Θ_G) is some K lower than Θ_{100} (Figure 1) and is determined by Newtonian iteration (Appendix A, Schumann, 1996). Increasing G leads to higher Θ_{100} and Θ_G . Supersaturation within a plume is generated earlier and becomes larger in a colder air mass since the end point of the mixing line is shifted toward a lower temperature (green line in Figure 1). According to equation (2), a larger atmospheric pressure leads to a larger G which also leads to an earlier onset and increase in maximum plume supersaturation.

2.2. Parametrized Contrail Ice Crystal Formation

Plume aerosol particles have varying sizes and properties with larger and more hygroscopic particles activating into droplets first (Köhler, 1936) depleting supersaturation (s_w). The basic assumption of the parameterization of Kärcher et al. (2015) is that all droplets in the rapidly cooling plume form at the same time, (t_o), at the “activation relaxation time.” The parameterization determines the droplet number concentration ($n(t_o) = n_o$) which is needed to balance a further increase of s_w by condensation loss. This implies two approximations: The first one is that quenching of s_w is assumed to occur instantly since the remaining smaller and less hydrophilic particles cannot be activated any more once s_w is decreasing. The second one is that slight changes in the evolution of relative humidity within the plume resulting from earlier activation events are neglected. This is a reasonable approximation since cooling rates in the aircraft plume are much larger than those in the free atmosphere and the mean dry core radii of the considered plume particles (i.e., soot and entrained atmospheric particles) have comparable magnitudes. The approximation would pose a problem if ultrafine volatile particles were included (see below). The two approximations may partly compensate each other.

The droplet number concentration n_o is calculated by

$$n_o = \varphi_s EI_s \frac{D_o \rho_o}{N_e} + \varphi_a \frac{T_a}{T_o} (1-D_o) n_a = n_{o,s} + n_{o,a} \quad (3)$$

with contributions from activated emitted soot (subscript “s”) and atmospheric particles entrained into the plume (subscript “a”). EI_s denotes the soot number emission index, T_a ambient temperature, n_a the

background aerosol particle number concentration, and D_o , ρ_o , and T_o correspond to the plume dilution factor, density, and temperature at t_o , respectively. The dilution factor D is defined as the proportion between the air-to-fuel ratio at the engine outlet (N_e) and that to a later plume age ($N(t) > N_e$) so that $D(t)$ decreases with time. φ_s and φ_a denote which fraction of soot and entrained ambient particles is activated into water droplets. Dry core radii $r_{act,l}$ of each particle type l that can activate into water droplets at certain plume supersaturation s_w are obtained from Kappa-Köhler theory (Petters & Kreidenweis, 2007) by

$$r_{act,l} = r_K \sqrt[3]{\frac{4}{27 \ln^2(s_w) \kappa_l}}, \quad (4)$$

where $r_K \sim 1$ nm is the fixed Kelvin radius and κ_l denotes the hygroscopicity parameter characterizing the water uptake and activation behavior of the particle type l depending on its chemical composition. Please note that we use the parameterization from Kärcher et al. (2015) but we calculate the dry core radius for activation according to Petters and Kreidenweis (2007). This means that we keep the factor $4/27$ under the third root consistent with prescribing the Kelvin radius.

Typical values of κ derived from laboratory measurements range between 0.5 and 1.4 for hydrophilic salts, between 0.01 and 0.5 for slightly to very hygroscopic organic species, and are zero for purely hydrophobic compounds (Petters & Kreidenweis, 2007). Following Kärcher et al. (2015), we assume fully soluble upper tropospheric background particles with an average κ_a of 0.5 and soot particles with a soluble volume fraction of 1% and an effective κ_s of 0.005. Equation (4) indicates that the smaller and less hygroscopic particles need higher plume supersaturations to be activated. Soot and entrained atmospheric particles are each characterized by a log-normal size distribution and the integration of the size distributions over all radii larger than $r_{act,s}$ or rather $r_{act,a}$ yields the activation fractions φ_s and φ_a , respectively.

After activation, the droplets freeze rapidly into ice crystals by homogeneous nucleation so that the initial ice crystal number concentration is approximately given by n_o . Since laboratory measurements indicate that soot particles are not efficient ice nuclei (Bond et al., 2013; Hoose & Möhler, 2012; Kärcher et al., 2007), ice crystal formation due to heterogeneous freezing is excluded.

As a measure for the number of nucleated contrail ice crystals per burnt fuel mass, we introduce the apparent emission index of ice (Kärcher et al., 2015)

$$AEI_i = \frac{N_e n_o}{\rho_o D_o}. \quad (5a)$$

Inserting equation (3) in equation (5a) and applying the ideal gas law $\rho_o = \frac{p_a}{R_d T_o}$ denoting p_a atmospheric pressure and R_d specific gas constant for dry air yields

$$AEI_i = \varphi_s EI_s + \varphi_a N_e R_d \frac{1-D_o}{D_o} \frac{T_a}{p_a} n_a = AEI_{i,s} + AEI_{i,a}. \quad (5b)$$

The advantage of using AEI_i instead of n_o is that, for soot-rich emissions ($AEI_{i,s} \gg AEI_{i,a}$), AEI_i is approximately given by the number of activated soot particles per burnt fuel mass and does not depend on plume dilution and air density. The second term is particularly relevant for soot-poor emissions ($EI_s < \sim 10^{13}$ (kg-fuel) $^{-1}$) and varies with the plume dilution at droplet formation time t_o . As D decreases and therefore $1-D$ increases with plume age, more atmospheric particles are entrained into the plume with increasing t_o so that more of these particles are potentially available for ice crystal formation.

We calculate the ice crystal number concentration of 120 s old contrails (n_i) by continuous dilution of n_o neglecting the vortex regime

$$n_i = \frac{n_o}{D_o} D_{(120s)}, \quad (6)$$

where the plume dilution factor is determined from Kärcher et al. (2015) by $D(t) = \left(\frac{0.01s}{t}\right)^{0.9}$ so that $D_{(120s)} \sim 2.13 \cdot 10^{-4}$.

For soot-poor emissions and at ambient temperatures of around 10 K below Θ_G , very large relative humidities over water ($>200\%$) are generated during mixing. Since the low number of emitted soot together with the ambient aerosol particles can no longer effectively quench supersaturation, ultrafine volatile particles can activate into water droplets and subsequently freeze (Kärcher & Yu, 2009). Since mean dry core radii of volatile particles are significantly lower than those of soot and ambient aerosol particles, volatile particles require much higher plume supersaturations in order to be activated into water droplets. Therefore, small changes in supersaturation caused by the prior activation of larger soot and ambient particles may affect the activation of volatile particles significantly. Nucleation of ultrafine volatile particles is therefore not covered by the parameterization of Kärcher et al. (2015) since the treatment of subsequent activation would require a more complex and computationally more expensive parameterization.

2.3. Offline Studies for Contrail Ice Crystal Formation

We investigate offline the apparent emission index of ice as defined by equations (5a) and (5b) for different soot number emissions depending on ambient temperature (section 3.1), air pressure (section 3.2), and altitude (section 3.3), the latter assuming temperature and pressure to vary in line with the international standard atmosphere. We prescribe two soot-rich emissions with a present-day “high soot case” ($EI_s = 1.5 \cdot 10^{15} \text{ (kg-fuel)}^{-1}$), based on in situ measurements of nonvolatile particles behind commercial aircraft (Anderson et al., 1998), and a “reduced soot case” ($EI_s = 3 \cdot 10^{14} \text{ (kg-fuel)}^{-1}$) decreasing high soot emissions by 80%. Furthermore, we investigate one soot-poor emission scenario with $EI_s = 10^{13} \text{ (kg-fuel)}^{-1}$. We restrict our study to ambient temperatures within about 10 K of the formation threshold (i.e., above 215 K at cruise altitudes) since for soot-poor emissions ice crystal formation on ultrafine particles cannot be neglected any longer. Vapor mass emission index, combustion heat, and propulsion efficiency, which influence the slope of mixing line (equation (2)), are fixed for a conventional airliner according to Schumann (1996). We exemplarily prescribe a constant relative humidity over ice (RH_i) of 120% lying well in between ice saturation and highly ice-supersaturated conditions needed for natural cirrus cloud formation (Koop et al., 2000). Decreasing (increasing) relative humidity to 100% (140%) leads to a decrease (increase) of Θ_G by around 1 K so that primarily the onset of contrail formation is shifted toward lower (higher) temperatures. Changing RH_i will have only a large impact on the initial ice crystal number if contrails form close to Θ_G while the variation in RH_i has hardly any influence if the formation threshold is well exceeded. Following Kärcher et al. (2015), we prescribe a log-normal distribution for soot and background aerosol particles and set the geometric-mean core radius to 15 nm for both particle types. The mean soot core size is deduced from observations in aircraft plumes at cruise altitudes (e.g., Moore et al., 2017; Petzold et al., 1999). We set a background aerosol particle number concentration of 600 cm^{-3} which can be seen as a typical value in the extra-tropical upper troposphere (Minikin et al., 2003; Stier et al., 2005).

2.4. Model Description and Simulations

2.4.1. ECHAM5-HAM and CCMoD

ECHAM5 is the fifth generation of the general atmospheric circulation model ECHAM (Roeckner et al., 2003, 2006) which has been extended by the aerosol module HAM (Stier et al., 2005). We use the contrail cirrus parameterization (CCMoD) based on Burkhardt and Kärcher (2009) which has been extended to a microphysical 2-moment scheme (Lohmann et al., 2008) by Bock and Burkhardt (2016a). Thereby, ice crystal number has been introduced as an additional prognostic variable which is, for example, necessary for investigating the effect of reduced soot number emissions. We simulate the formation of persistent contrails when the SA-criterion (Schumann, 1996) is fulfilled (section 2.1) and a fraction of the grid box is ice-supersaturated. The fractional ice-supersaturated but cloud-free area of the grid box is parameterized according to Burkhardt et al. (2008) consistent with the natural cloud scheme (Sundqvist, 1978). The resulting ice-supersaturation frequency compares well with observations (Bock & Burkhardt, 2016a; Lamquin et al., 2012). ECHAM5-CCMoD is complemented in this paper by the parameterization of contrail ice crystal formation, which is mainly dependent on soot number emissions and atmospheric state (Kärcher et al., 2015), described in section 2.2. When contrails form in the grid box, ice nucleation occurs within the fractional contrail volume which is calculated from the contrail length (fraction of air traffic flight distance forming a contrail) and the mean cross-sectional contrail area.

2.4.2. Global Simulations and Setup

For our global simulations with ECHAM5-CCMod, described in section 4, we use a horizontal resolution of T42 which translates in the midlatitudes into a geometric dimension of the Gaussian grid boxes of about 300×200 km (latitude \times longitude). We use a model configuration with 41 vertical layers (16 above 200 hPa and 25 below) because of the increased vertical resolution, about 500 m, near the tropopause (Kurz, 2007). The time step of the model is 15 min.

Air traffic for the year 2006 is defined using the AEDT flight inventory (Wilkerson et al., 2010). As in the offline calculations, we prescribe a geometric-mean soot particle core radius of 15 nm. Number concentrations and geometric-mean particle sizes for the ambient aerosol particles are obtained from the aerosol module HAM (Stier et al., 2005).

We have performed one simulation with high soot and the other with 80% reduced soot number emissions. Since the parameterization of Kärcher et al. (2015) does not account for ice nucleation on ultrafine volatile particles (section 2.2) and can therefore not be used for estimating ice nucleation for soot-poor emissions, we do not perform simulations for the soot-poor emission case. Both simulations have been run for 5 years. We investigate the apparent emission index of ice (defined by equations (5a) and (5b)); the ice crystal number per flight distance (N_{FD}), taking into account the variability in fuel consumption; and the total nucleated ice crystal number per volume air (N_{tot}) accounting for air traffic density and contrail formation probability. We limit our study to contrail ice crystal formation and do not analyze resulting contrail cirrus fields. Our analysis is performed on model levels for which we give the approximate pressure levels.

3. Sensitivity Studies for Contrail Ice Crystal Formation

In this section, we investigate the impact of varying atmospheric conditions on contrail ice crystal formation offline for three different soot number emissions. We analyze the sensitivity of the nucleated ice crystal number on ambient temperature (as in Kärcher et al., 2015), on air pressure, and on flight altitude, varying both temperature and air pressure at fixed ice-supersaturated conditions. We analyze when changes in the nucleated contrail ice crystal number are most sensitive to changes in soot number emissions and study in more detail the influence of entrained background aerosol particles for soot-poor emissions.

3.1. Temperature Dependency

Figure 2a shows the apparent emission index of ice depending on temperature for three different soot number emissions. Prescribing a relative humidity over ice of 120% and an atmospheric pressure of 240 hPa yields a SA-threshold temperature (Θ_G) of around 225.5 K. There is a strong nonlinear relationship between the number of formed contrail ice crystals and ambient temperature close to the contrail formation threshold (i.e., when temperature is within 3 K of Θ_G). At threshold conditions where temperature is only one tenth K below Θ_G , maximum plume supersaturation does not exceed 1%. Due to the poor water-solubility of soot particles, only few large particles can activate into water droplets. The apparent emission index of ice (AEI_i) increases steeply with decreasing temperature down to 222.5 K where maximum plume supersaturation reaches nearly 20% and around half of the emitted soot particles can activate into droplets for the high soot case (black) and 65% for the reduced soot case (red). At temperatures far away from the SA-threshold (i.e., below around 220 K or temperature difference to $\Theta_G > 5$ K), AEI_i slowly approaches the soot number emission index and more than 80% of emitted soot particles can form ice crystals. Ice crystal number concentration of 120 s old contrails, calculated by equation (6), behaves analogously to AEI_i and approaches around $1,500 \text{ cm}^{-3}$ for the high soot and 350 cm^{-3} for the reduced soot case at lower temperatures (dashed lines in Figure 2a).

The number of nucleated ice crystals decreases nearly proportionally with soot number emissions reduced by 80% at temperatures far away from the SA-threshold (red line in Figure 2b). The decrease in AEI_i is slightly below 80% because the fraction of soot particles forming ice crystals is higher for lower soot number emissions. This decrease weakens further when approaching near-threshold conditions. Only very close to the SA-threshold (i.e., at temperatures within 0.2 K of Θ_G), the impact of reduced soot emissions on nucleated ice crystal number is significantly diminished and AEI_i decreases by less than 50–60%. This is because at low plume supersaturations ($< 1\%$), it is to a large degree the more hygroscopic ambient aerosol particles entrained from the environment that activate into water droplets and subsequently freeze into ice crystals.

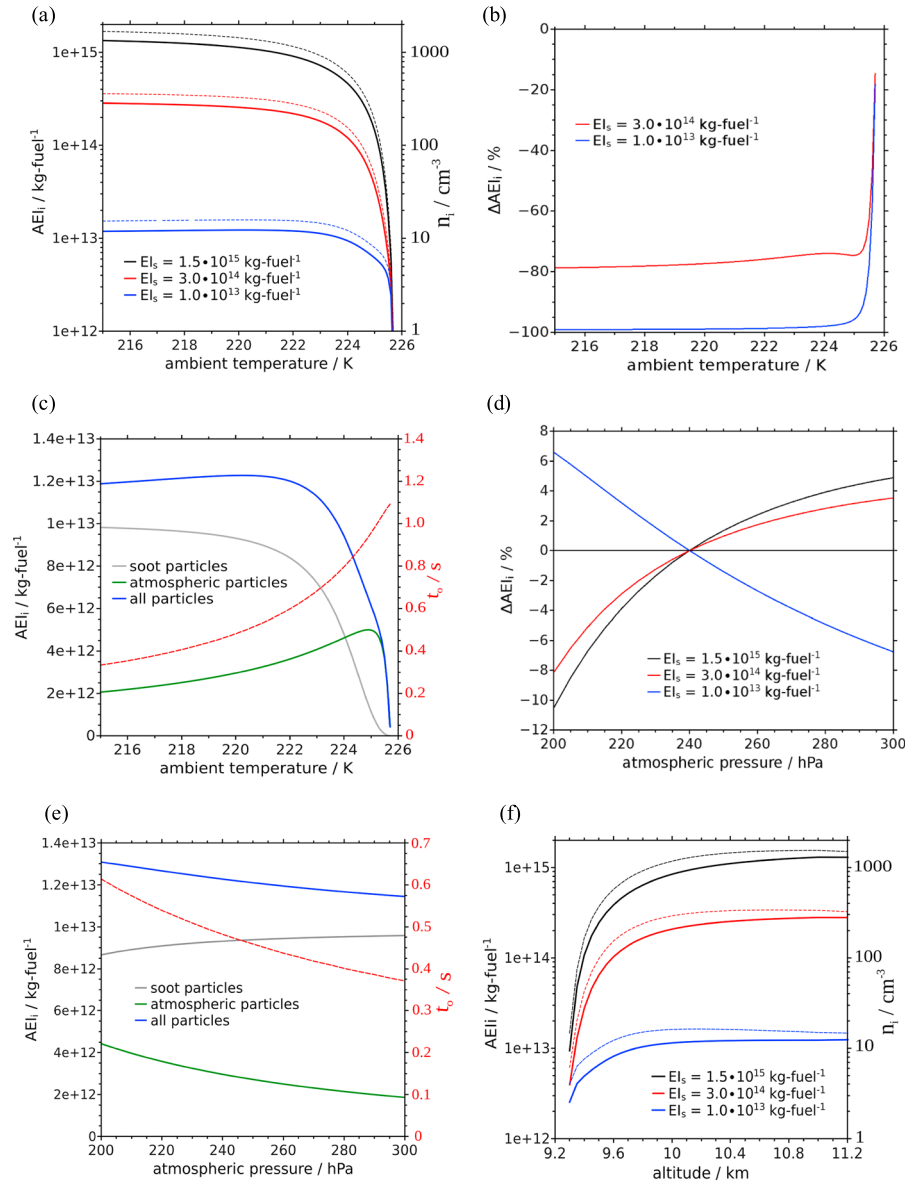


Figure 2. Apparent emission index of ice (AEI_i) depending on (a–c) ambient temperature, (d and e) atmospheric pressure, and (f) altitude, assuming temperature and pressure values from the standard atmosphere (ISO 2533:1975). (a), (d), and (f) show AEI_i for three different soot number emission indices (EI_s) depicted in the labels; the dashed lines in (a) and (f) indicate the ice crystal number concentration at a contrail age of 120 s with axis labeling on the right side. (b) illustrates the percentage change of AEI_i due to 80% (red) and 99% (blue) reduced soot emissions with respect to the high soot case ($EI_s = 1.5 \cdot 10^{15} \text{ (kg-fuel)}^{-1}$); (c) and (e) depict AEI_i only for $EI_s = 10^{13} \text{ (kg-fuel)}^{-1}$ (blue) showing the contributions by the activated soot and activated entrained atmospheric aerosol particles dependent on atmospheric temperature and pressure, respectively; the red dashed lines in (c) and (e) indicate the activation relaxation time (t_a) for the soot-poor case. Relative humidity over ice is fixed to 120%; pressure in (a)–(c) and temperature in (d) and (e) are set to 240 hPa and 220 K, respectively.

In our soot-poor emission scenario ($EI_s = 10^{13} \text{ (kg-fuel)}^{-1}$), AEI_i also increases steeply from the threshold case reaching a maximum at 220 K and then decreases by around 3% at 215 K relative to the maximum. To explain the slight decrease in the nucleated ice crystal number below 220 K, Figure 2c shows AEI_i for the soot-poor emission and the contributions from the activated soot ($AEI_{i,s}$) and entrained ambient aerosol particles ($AEI_{i,a}$). As for soot-rich emissions (Figure 2a), $AEI_{i,s}$ approaches EI_s at temperatures far away from the SA-threshold. $AEI_{i,a}$ first increases with decreasing temperature down to 225 K. The subsequent decrease

in $AEI_{i,a}$ is explained by the fact that droplets form some tenths of a second earlier with decreasing temperature (red line in Figure 2c) since plume supersaturation is generated earlier (Figure 1). Consequently, less ambient aerosol particles are mixed into the exhaust at this time as indicated by equation (5b). Since in the soot-poor emission case the number of entrained aerosol particles and the emitted soot particle number have a comparable magnitude, the maximum AEI_i is around 23% larger than the soot emission index and the decrease in $AEI_{i,a}$ can be seen in the overall apparent emission index of ice at atmospheric temperatures far away from the SA-threshold.

Due to our correction of the transcription error in equation (4) introduced in section 2.2, our temperature dependency of AEI_i quantitatively differs to that in Figure 12a from Kärcher et al. (2015) particularly near the contrail formation threshold.

3.2. Pressure Dependency

Figure 2d shows the percentage change of the apparent emission index of ice when varying atmospheric pressure relative to 240 hPa and prescribing a constant ambient temperature of 220 K for the three different soot number emissions. When increasing pressure to 300 hPa, AEI_i rises by around 5% and 4% for the high (black) and reduced soot case (red), respectively. This is because the slope of the mixing line defined in equation (2) is steeper at a higher pressure leading to a larger plume supersaturation. The change of AEI_i becomes larger with decreasing pressure (from 240 to 200 hPa) because contrails form closer to the SA-threshold (due to a lower Θ_G with decreasing slope of the mixing line).

For our soot-poor emission scenario, the pressure dependency of ice crystal formation behaves inversely to that at soot-rich emissions. Decreasing (increasing) pressure to 200 hPa (300 hPa) leads to an increase (decrease) in AEI_i by around 6%. To understand this behavior, we show in Figure 2e the apparent emission index of ice for our soot-poor emission subdivided into the contributions by activated soot ($AEI_{i,s}$) and entrained ambient aerosol particles ($AEI_{i,a}$). As in the soot-rich cases, $AEI_{i,s}$ increases slightly with rising pressure. In contrast, $AEI_{i,a}$ clearly decreases if pressure is increased. Similar to lowering ambient temperature, increasing pressure causes droplet formation to occur a few tenths of a second earlier (red line in Figure 2e) because supersaturation within the plume is generated earlier (Figure 1). At that time, fewer aerosol particles from the environment have been entrained into the jet plume so that fewer of these particles are available for ice crystal formation. Similar to the argument in the previous section, the change in the overall apparent emission index of ice basically results from the pressure dependency of $AEI_{i,a}$.

3.3. Height Dependency

Changes in flight levels (resulting in a change in pressure and temperature) are often discussed in connection with mitigation of contrails or in general with the climate impact of air traffic. Therefore, we investigate the dependency of the number of formed contrail ice crystals on altitude (Figure 2f). Assuming that pressure and temperature vary in line with the international standard atmosphere (International Organization for Standardization, 1975), and prescribing an ambient relative humidity over ice of 120%, independent of height, the SA-criterion is fulfilled at altitudes higher than 9.3 km. Near the contrail formation threshold (i.e., until 9.8 km or 270 hPa), AEI_i (solid) and ice crystal number concentration (dashed) increase steeply with rising altitude for all soot emissions. This is because more plume particles can be activated into droplets as temperature is decreased and therefore maximum plume supersaturation is increased. The subsequent increase in the nucleated ice crystal number weakens and AEI_i approaches the soot emission index at around 10.5 km (245 hPa) for soot-rich emissions where more than 80% of emitted soot particles can form ice crystals. In our soot-poor emission scenario (blue), AEI_i rises more weakly with increasing altitude near the SA-threshold than for soot-rich emissions and slightly increases further above 10 km. We deduce from these results that the contrail ice crystal formation dependency on height is dominated by the temperature effect for soot-rich emissions. The increasing altitude would lead to a decrease in AEI_i if the temperature impact was neglected (Figure 2d).

4. Frequencies and Global Distribution of Contrail Ice Nucleation

We simulate the ice crystal formation in contrails globally with ECHAM5-CCMod. First we study how often contrails are formed when ambient temperature is close or well below the SA-threshold (section 4.1). We then investigate the spatial distribution of the nucleated ice crystal number of contrails for high soot

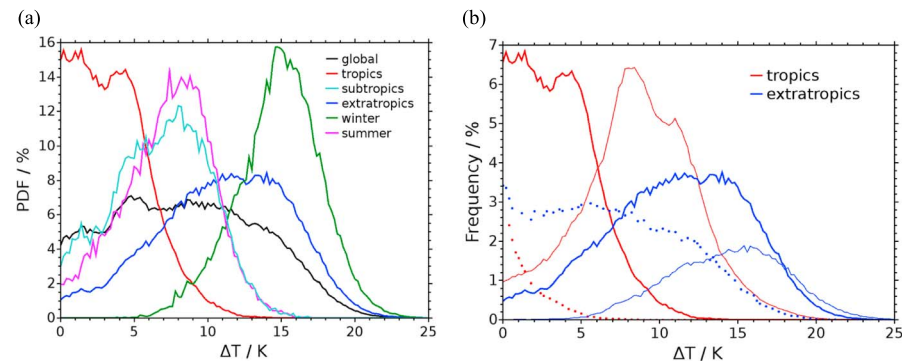


Figure 3. (a) PDF of the temperature difference (ΔT) between ambient temperature and the SA-threshold temperature around the cruise level (between 210 and 250 hPa) for the whole globe (black), the tropics (red, 25°S–25°N), northern subtropics (cyan, 25–40°N) and northern extratropics (blue, 40–70°N) for the whole year as well as for the northern extratropics for winter (green) and summer (magenta) only; (b) contribution of three different altitude ranges to the PDF of ΔT between 150 and 350 hPa for the tropics and extratropics: The thin line represents 150–210 hPa, the thick solid line 210–250 hPa and the dots 250–350 hPa. The PDFs and frequencies are calculated for states that enable formation of persistent contrails. PDF = probability density function.

number emissions and its seasonal variability (section 4.2). Finally (in section 4.3), we analyze the impact of 80% reduced soot number emissions on contrail ice crystal formation. The soot-poor emission case is not investigated since the parameterization of Kärcher et al. (2015) does not account for ice nucleation on ultrafine volatile particles (sections 2.2 and 2.4.2).

4.1. Temperature Distribution Relative to Formation Threshold

We investigate how frequently contrails form and how often they form close to the SA-threshold. For a better understanding of the spatial and temporal distribution of contrail ice crystal formation we distinguish between different latitudinal regions, seasons, and altitude. We analyze only persistent contrail formation within ice-supersaturated air masses since only these contrails can be highly climate relevant.

Figure 3a shows the probability density function (PDF) of the temperature difference (ΔT) relative to the threshold temperature, Θ_G , at altitudes close to the cruise level (between 210 and 250 hPa). Globally, approximately 12% of aircraft flown distance forms persistent contrails (Table 1). Most of those contrails form far below the SA-threshold (with the highest frequencies of ΔT between 5 and 12 K), and only 15% of contrails develop at near-threshold conditions. This distribution mainly reflects the distribution in the northern extratropics and subtropics where air traffic density is much higher than in the tropical regions (Newinger & Burkhardt, 2012). In the extratropics, approximately 14% of aircraft flown distance forms persistent contrails. The contrail formation threshold is in about 90% of cases well exceeded ($\Delta T > 5$ K) and most of the contrails form at temperatures 9–15 K below Θ_G . During summer, persistent contrails form slightly less frequently and the maximum frequency of ΔT is shifted to around 7–10 K. In winter the maximum frequency of ΔT is located at around 14–17 K. In contrast, in the tropics and in the northern subtropics persistent contrail formation is less likely; around 45% and 14% of contrails form near the SA-threshold (i.e., $\Delta T < 3$ K, section 3.1) and maximum frequencies of ΔT lie between 0 and 5 K and 5 and 10 K, respectively.

Figure 3b shows the sensitivity of contrail formation on altitude. We analyze the contributions of three different height layers (ranging between 150 and 350 hPa) first to the contrail formation frequency in general and second to the PDF of ΔT , both for the tropical and the northern extratropical regions.

In the extratropics, 45% of persistent contrails develop at cruise altitudes, 38% between 250 and 350 hPa, and 17% of contrails form above 210 hPa. Above 210 hPa, contrails are most likely to form at temperatures of 12–18 K below Θ_G and nearly no contrails form at temperatures within 5 K of Θ_G . While less than 5% of persistent contrails form near their formation threshold around cruise level (210–250 hPa), the amount of near-threshold contrails increases to around 22% at altitudes below 250 hPa but the SA-threshold is still well exceeded ($\Delta T > 5$ K) for the majority of persistent contrails.

Table 1

Annual Mean Temperature Bias in the Global Climate Model (T_{bias}) Relative to ERA-Interim Data at Cruise Altitudes (210–250 hPa); Probability of Persistent Contrail Formation (P_{form}) and of Contrail Formation Close to the Schmidt-Appleman-Threshold ($\Delta T < 3$ K; P_{NTH}), Apparent Emission Index of Ice (AEI_i), Grid-Mean Ice Number Concentration (N_{tot}), and In-Cloud Ice Number Concentration (n_i) of 120 s Old Contrails Averaged Over the Whole Globe, Northern Extratropics (40–70°N), Northern Extratropics Only During Summer, Northern Subtropics (25–40°N), and the Tropics (25°S–25°N)

Region/Season	T_{bias} (K)	P_{form} (%)	P_{NTH} (%)	AEI_i (10^{15} kg $^{-1}$)	N_{tot} (m $^{-3}$)	n_i (cm $^{-3}$)
Global	−3.5	11.9 (9.8)	1.76 (2.22)	1.23 (1.12)	0.52 (0.39)	1455 (1325)
Extratropics	−4.5	13.8 (12.6)	0.63 (1.74)	1.34 (1.20)	1.72 (1.40)	1587 (1422)
Summer	−4.0	13.3 (11.3)	1.29 (3.68)	1.20 (0.96)	1.43 (0.97)	1430 (1144)
Subtropics	−2.5	10.7 (9.4)	1.47 (2.05)	1.16 (1.03)	0.94 (0.74)	1360 (1210)
Tropics	−2.5	9.4 (5.8)	4.61 (3.62)	0.87 (0.70)	0.09 (0.04)	1027 (821)

Note. The numbers in parentheses represent the values after offline temperature bias correction of the model. The calculation of these quantities and the bias correction are described in Appendix A.

In the tropics, around 52% of the persistent contrails develop above 210 hPa, 44% near the cruise level, and only 4% below 250 hPa. Figure 3b shows that contrails in the tropics form predominantly far away from their formation threshold at altitudes above 210 hPa whereas around 45% of contrails in the tropics around the cruise level (210–250 hPa) form at temperatures within 3 K of Θ_G . Contrail formation below 250 hPa in the tropics is extremely unlikely and, if contrails form, most of them are near-threshold cases. Persistent contrail formation in this area occurs rarely not because ice-supersaturation frequency is low but because the temperature threshold for contrail formation is seldom exceeded (Burkhardt et al., 2008).

As in many climate models, the tropopause in our model is too high in the extratropics, so that ice-supersaturation frequency is overestimated (Lamquin et al., 2012), and ambient temperature is underestimated in the upper troposphere (Hertwig et al., 2015; Roeckner et al., 2006). As a consequence of the too high tropopause, the formation of persistent contrails in our climate model is overestimated in particular in the extratropical upper troposphere, at about 150–200 hPa. Due to the upper tropospheric temperature bias, we overestimate contrail formation probability and underestimate the number of near-threshold cases. This is in particular the case in the tropics around cruise altitudes and below, in the subtropics over the southeastern United States and in some northern extratropical regions during summer. Applying offline a constant temperature bias correction at cruise altitudes (Appendix A), persistent contrail formation probability decreases globally from around 12% to 10% and the probability that contrails form near the SA-threshold increases from 1.8% to 2.2% (Table 1). In the tropics, the probability for contrail formation and for near-threshold contrail formation ($\Delta T < 3$ K) changes from 9.4% to 5.8% and from 4.6% to 3.6%, respectively. Due to the large decrease in contrail formation probability, the slight decrease in the probability of near-threshold formation translates into a large percentage increase (from 45% to around 60%) when seen relative to the number of contrails forming. In the northern subtropics and extratropics, changes are slightly smaller. The probability of persistent contrail formation in the northern subtropics is reduced by 1.3 percentage points (pp) and near-threshold cases are slightly increased by about 0.6 pp. The respective numbers in the northern extratropics are 1.2 and 1.1 pp (Table 1).

4.2. Spatial Variability of Contrail Ice Nucleation

Here we study the spatial variability of the number of formed contrail ice crystals, when prescribing present-day soot emissions ($EI_s = 1.5 \cdot 10^{15}$ (kg-fuel) $^{-1}$), including its seasonal variability and height dependency in case of persistent contrail formation.

4.2.1. Apparent Emission Index of Ice

Figure 4a shows the annual mean apparent emission index of ice (AEI_i) at about 240 hPa (i.e., near the main cruise level at 230 hPa). North of 50/60°N and south of 45°S AEI_i is close to the soot number emission index (EI_s) which means that more than 90% of emitted soot particles are activated into water droplets and subsequently freeze. This is because in those areas the ambient temperature is at least 8 K below the SA-threshold temperature (Θ_G ; Figure 4b). AEI_i is reduced by around 20–35% relative to EI_s between 30/40°N and 50°N over the eastern United States, eastern Asia, as well as over the Atlantic and Pacific Ocean. In the tropics, contrail formation at about 240 hPa is not as common as in the extratropics (contour lines in Figure 4a) and a high fraction of persistent contrails form near the formation threshold, that is,

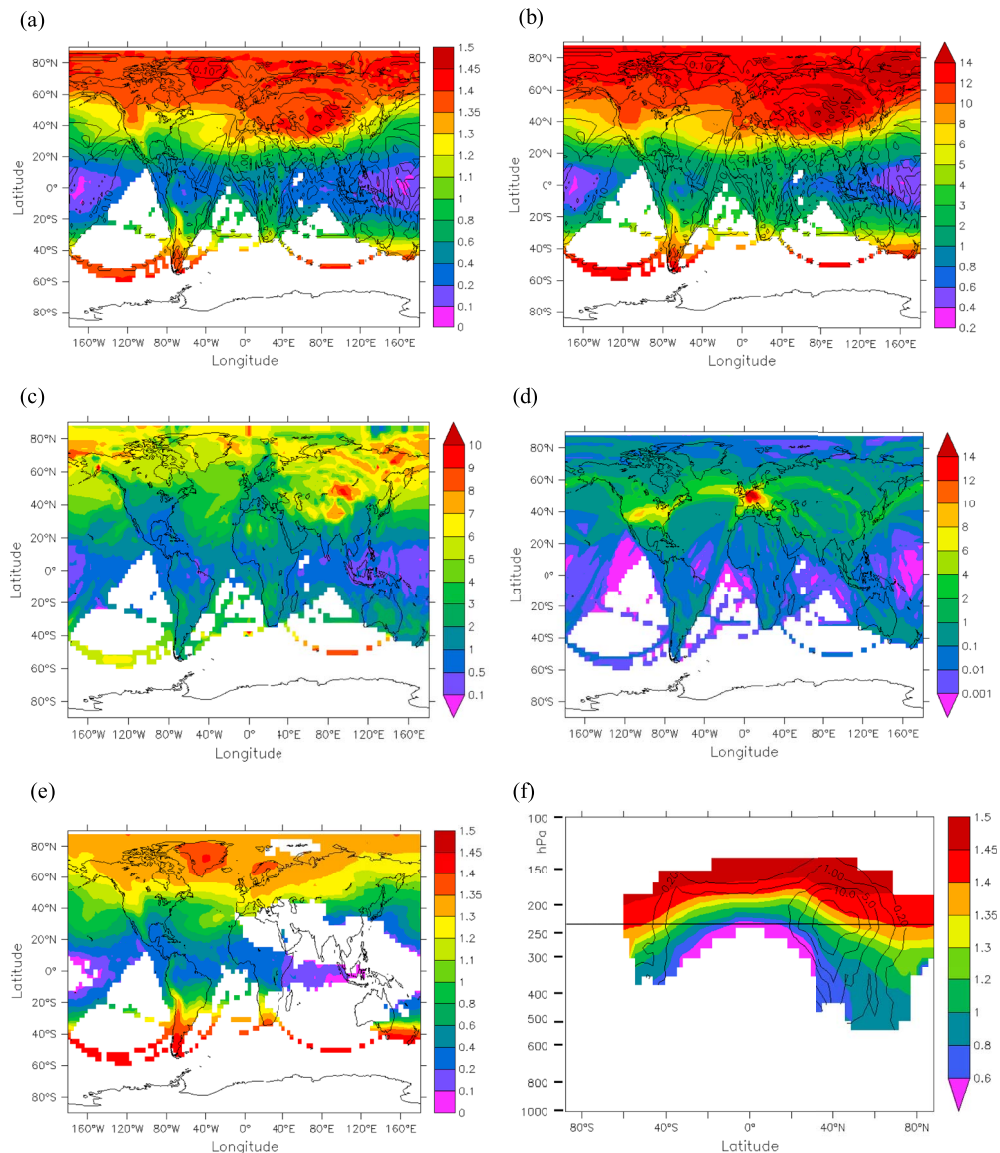


Figure 4. Global distribution of the annual mean (a) apparent emission index of ice in $10^{15} \text{ (kg-fuel)}^{-1}$, (b) difference between SA-threshold temperature and ambient temperature in K; the number of nucleated contrail ice crystals (c) per flight distance in 10^{12} m^{-1} and (d) per air volume in m^{-3} at about 240 hPa. (e) shows the apparent emission index of ice (in $10^{15} \text{ (kg-fuel)}^{-1}$) for the northern hemispheric summer months at about 240 hPa and (f) depicts the vertical profile of the zonal mean apparent emission index of ice in $10^{15} \text{ (kg-fuel)}^{-1}$. The averages are conditional on the formation of persistent contrails. The black contour lines in (a), (b), and (f) indicate the contrail formation frequency (product of flight distance and contrail formation probability). The straight line in (f) symbolizes the main cruise level at 230 hPa.

$\Delta T < 3 \text{ K}$ (section 4.1). Therefore, ice crystal formation is significantly limited by the maximum water supersaturation within the engine plume (Kärcher et al., 2015) and, consequently, AEI_i is frequently reduced by more than 60% relative to EI_s . Over the equatorial Pacific and Indonesia, ambient temperatures at contrail formation are often within 0.5 K of the threshold temperature so that on average only 10–25% of the emitted soot particles can form ice crystals. Please note that the higher values of AEI_i over the Andes and over Central Africa are an artifact of analyzing ice nucleation on model levels since model levels are slightly elevated over high mountains.

In the main air traffic areas contrail ice nucleation is slightly or moderately affected by atmospheric conditions as air traffic is particularly located in the northern extratropics (Newinger & Burkhardt, 2012). Of the

regions with high flight density, AEI_i is reduced strongest (by around 20–30%) over the southeastern United States and eastern Asia due to higher ambient temperatures.

As explained in section 3.1, the fraction of soot particles forming ice crystals increases with decreasing soot number emissions. Consequently, for reduced soot emissions, the areas in the northern extratropics where AEI_i is close to EI_s would move further south comprising Europe and the North Atlantic (not shown).

Ice crystal number density of 120 s old contrails (n_i , not shown) ranges between around 1,500 and 1,700 cm^{-3} over Europe and the northern United States and lies between 1,200 and 1,500 cm^{-3} over the eastern and southern United States. Due to the relatively frequent contrail formation close to the SA-threshold, n_i is significantly lower in the tropics displaying minima of 100–200 cm^{-3} over the equatorial Pacific and of around 300 cm^{-3} over Indonesia. Note that these ice number densities are not directly comparable with in situ measurements of young contrails since we do not account for the vortex regime. Assuming an ice crystal loss during the vortex phase on the order of 50%, a typical value for upper tropospheric temperatures (around 215 K) and moderately ice-supersaturated conditions (Unterstrasser, 2016), our calculated n_i in the northern extratropics would be in good agreement with measured ice crystal number densities of few minute old contrails over central Europe (Febvre et al., 2009; Schröder et al., 2000; Voigt et al., 2010).

Applying a constant correction for the temperature bias, as in section 4.1, leads around cruise altitudes to a further decrease in spatially averaged AEI_i and n_i by around 20% in the tropics, by 11% in the northern subtropics, by 10% in the northern extratropics, and by 20% in the northern extratropics during summer, respectively (Table 1).

4.2.2. Variability in Nucleated Ice Crystal Number per Flight Distance and Air Volume

Here we investigate the variability in the total number of nucleated contrail ice crystals per flight distance and per air volume, taking into account not only the variability in the apparent emission index of ice but also the variability in fuel use and in air traffic density, as given by the AEDT air traffic inventory (Wilkerson et al., 2010), and in contrail formation probability.

The initial ice crystal number per flight distance (N_{FD}), the product of aircraft fuel consumption and the apparent emission index of ice, is shown in Figure 4c at about 240 hPa. The fuel consumption of airplanes is largest in long-haul flights due to the huge take-off weight of bigger aircraft types and the higher amount of fuel needed. Therefore, we find the largest values of N_{FD} ($>5\text{--}6\cdot 10^{12} \text{ m}^{-1}$) within the North Pacific routes and over some parts of Asia and also relatively high values in the Atlantic flight routes between Europe and Mexico/South America. N_{FD} is considerably smaller over the equatorial Pacific than over the northern and southern Pacific because contrails form near their formation threshold and the ice crystal formation on soot particles is strongly limited (Figure 4a). Over Europe and the United States fuel consumption and, therefore, N_{FD} are relatively low ($<2\text{--}3\cdot 10^{12} \text{ m}^{-1}$) since air traffic is dominated by short-haul flights of smaller airplanes.

On the other hand, air traffic density over Europe and the United States is much higher than in other regions. As a consequence, we find maximum values in the total contrail ice crystal number per air volume (N_{tot}) over central Europe and the eastern United States (Figure 4d) despite lower fuel consumption. Relatively high values of N_{tot} can also be found over the North Atlantic flight routes and some areas in eastern Asia, comprising eastern China, Korea, and Japan. Despite similar contrail formation frequency (contour lines in Figure 4a) between eastern Asia and western Indonesia N_{tot} is significantly lower in the latter region since AEI_i is considerably reduced (section 4.2.1).

Applying a constant correction for the temperature bias around cruise altitudes, as in section 4.1, leads to a correction in N_{tot} by around 50% in the tropics, by around 20% in the northern subtropics and extratropics, and by 32% in the northern extratropics only during summer (Table 1). The decrease in the overall ice crystal number results both from the overestimation in the contrail formation probability and from the overestimation in AEI_i .

4.2.3. Seasonal Variability

Figure 4e shows the apparent emission index of ice (AEI_i) at about 240 hPa averaged over the northern hemispheric summer months only. The fraction of soot particles forming ice crystals is decreased down to 80% in the extratropics north of 50/60°N. Significant differences to the annual mean can be seen over the eastern Pacific, eastern Asia, and large parts of the southeastern United States where AEI_i is decreased by around

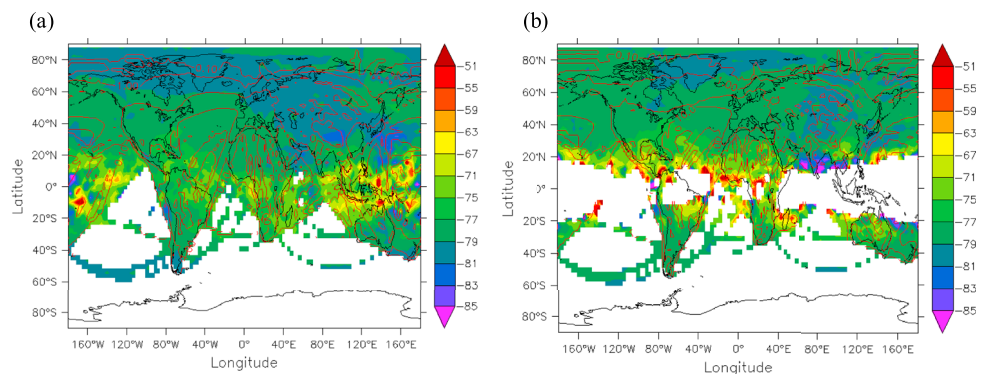


Figure 5. Percentage change of the annual mean apparent emission index of ice due to 80% reduced soot number emissions at about (a) 240 and (b) 260 hPa. The red contour lines indicate the contrail formation frequency (product of flight distance and contrail formation probability). Averages are conditional on the formation of persistent contrails. Differences in the number of formed ice crystals are statistically significant in almost all grid boxes at the 99% level.

30–70% relative to EI_s . This is because contrails form more frequently close to the SA-threshold (Figure 3a). In certain tropical and subtropical areas, particularly over southern Asia, contrails are not able to form due to higher ambient temperatures (above Θ_G) in the summer months. Near-threshold contrails tend to develop more frequently over central Africa and the Indian Ocean compared to the annual mean.

4.2.4. Height Dependency

Figure 4f shows the height profile of the zonal and annual mean apparent emission index of ice. If contrails form, more than 95% of emitted soot particles can form ice crystals above around 200–220 hPa in the extratropics and above 180 hPa in the tropical regions. Note that for reduced soot emissions, the altitude from which AEI_i is close to EI_s would move further downwards.

Ice nucleation at the main cruise level (indicated by the straight line) is on average reduced by around 40–50% in the tropics, by around 25% in the subtropics, and by around 10% in the northern extratropics relative to EI_s . Persistent contrail formation is unlikely below 260 hPa in the tropics and below 300 hPa in the subtropics (contour lines in Figure 4f) and, if contrails form, AEI_i is strongly reduced, that is, by more than 75% in the tropics and by more than 50% in the subtropics relative to EI_s . This reduction of AEI_i at lower altitudes is smaller in the northern extratropics and amounts to around 30% at 300 hPa and 45% at 400 hPa. Below 400 hPa in the extratropics, persistent contrail formation is quite rare as ice-supersaturation frequency is low (<10–15%, Lamquin et al., 2012), but AEI_i is not further reduced.

Correcting for the upper tropospheric temperature bias in the model, we expect an upward shift of the lowest altitude where contrails form by around 20 hPa.

4.3. Impact of Reduced Soot Number Emissions

As explained in section 3.1, there is not necessarily a linear relationship between the number of nucleated ice crystals and soot number emissions (Figure 2b). In the following, we investigate the influence of a reduction of soot number emissions by 80% on ice nucleation.

Figure 5a shows the geographical distribution of the percentage change in the apparent emission index of ice (AEI_i) due to reduced soot emissions at about 240 hPa. In the extratropics, AEI_i is decreased nearly by the same degree as the soot number emission index since contrails typically develop far away from the SA-threshold. The slightly weaker decrease in AEI_i is because the fraction of soot particles forming ice crystals is higher for reduced soot emissions (section 3.1). In the tropics, the relative reduction of AEI_i is frequently below 75%. Over Indonesia and the Indian Ocean, the mean temperature difference to the SA-threshold temperature (Θ_G) is lower than 0.5 K (Figure 4b) so that the nucleated ice crystal number is often reduced by less than 70% or 60%. This is because at temperatures very close to the SA-threshold it is to a large degree the more hygroscopic ambient aerosol particles entrained into the plume that form ice crystals (see section 3.1). The reduction in the nucleated ice crystal number tends to decrease at a lower altitude (260 hPa) in the subtropics and tropics but persistent contrail formation in the tropics is still occasionally

possible (Figure 5b). Globally, AEI_i is reduced by close to 80% both at 240 and 260 hPa. This is because the majority of air traffic occurs in the northern extratropics where the number of nucleated ice crystals decreases almost at the same rate as the emitted soot particle number. The variability in the change of AEI_i is particularly large in areas where contrails form infrequently (contour lines in Figure 5) so that averages are made of few contrail formation incidents. In those areas reductions may also exceed 80% due to the fact that the meteorology in the two simulations is not identical.

5. Conclusions and Outlook

We analyze the variability in contrail ice nucleation with the background atmospheric state and its dependence on soot number emissions. Ice nucleation within contrails is limited, on the one hand, by the number of emitted soot particles and, on the other hand, by the maximum plume water supersaturation which is mainly determined by the difference between ambient temperature and the contrail formation threshold temperature (Kärcher et al., 2015). There are a number of possibilities to reduce engine soot number emissions, for example, by mixing conventional Jet-A fuel with a biofuel (Moore et al., 2017). Bier et al. (2017) and Burkhardt et al. (2018) have shown that the contrail ice crystal number at initialization can have a strong impact on the life cycle and optical properties of contrail cirrus in large-scale and long-lived ice-supersaturated areas. The dependency of contrail ice nucleation on the background atmosphere has until now never been considered when simulating the life cycle of contrail cirrus. Here we study where and how frequently contrails form near the formation threshold and how strongly the number of nucleated ice crystals is decreased as compared to the emitted soot particle number. We investigate the dependency of contrail ice nucleation on soot number emissions for different climatic conditions.

Assuming that pressure and temperature vary in line with the international standard atmosphere, we find that in the extratropics, for present-day soot emissions, ice nucleation is mainly controlled by the change in temperature when changing altitude. The number of formed ice crystals per burnt fuel mass is clearly decreased at altitudes below 270 hPa (around 10 km) as contrails form close to their formation threshold due to higher ambient temperature. When reducing soot number emissions drastically to around 10^{13} (kg-fuel) $^{-1}$, ice nucleation increases more weakly with rising altitude.

Analyzing the spatial variability in contrail ice nucleation, we find that in the northern extratropics contrails form very frequently far away from threshold conditions. Therefore, the majority of emitted soot particles (on average around 90% at cruise levels and more than 70% between cruise altitude and 300 hPa) can form contrail ice crystals. In the tropics around cruise altitudes a large fraction of persistent contrails form close to the formation threshold and the number of soot particles forming ice crystals is on average reduced by about 50% relative to soot number emissions. This reduction in the tropics is clearly increased at lower flight altitudes but in those areas persistent contrails are unlikely to form. Of the main air traffic areas, it is mainly the southeastern United States and eastern Asia where ice nucleation is significantly reduced relative to soot number emissions due to the atmospheric state. This reduction is clearly enhanced during the summer months. While the impact of the meteorological situation on contrail ice crystal formation at cruise altitudes is significant in the tropics, it is on average low in the extratropics. This means that previous model estimates of contrail cirrus properties and radiative forcing do not suffer from large biases in contrail cirrus properties when neglecting the dependence of the formed ice crystal number on the atmospheric state. Only in the tropics and over the southeastern United States and eastern Asia the bias is expected to be significant.

Switching to alternative fuels has the largest impact on ice crystal formation at and above cruise altitudes in the extratropics and at altitudes above around 200 hPa in the tropics since in those areas the number of formed contrail ice crystals decreases nearly at the same rate as the soot number emissions. But even if atmospheric conditions limit the number of ice crystals forming on soot, the effect of alternative fuels is still significant. Only at atmospheric temperatures within a few tenths of K below the threshold temperature, the impact of changed soot emissions is strongly diminished. On the other hand, in those conditions contrail cirrus are unlikely to be climate relevant due to their low optical depth and short lifetime.

We have studied the spatial and temporal variability in contrail ice nucleation for present-day soot emissions and for a soot emission reduction of less than one order of magnitude. In the future, it will be important to estimate contrail ice nucleation for fuels with which it will be possible to reduce current soot number

emissions by more than one order of magnitude. If those fuels consist of sulfur or organic compounds, ice crystal formation on ultrafine volatile particles needs to be considered (Kärcher & Yu, 2009). Furthermore, the impact of the sinking vortices behind the airplane on the sublimation of ice crystals (Unterstrasser, 2016) needs to be considered since contrail properties and their life cycle are strongly impacted by the number of surviving ice crystals (Burkhardt et al., 2018).

Appendix A: Temperature Bias Correction

The upper tropospheric temperature bias (T_{bias} , Table 1) has been determined by comparing annual mean atmospheric temperature from the model output with 5 years averaged temperature data from ERA-Interim both globally and for different latitudinal regions, as indicated in Table 1, at cruise altitudes (210–250 hPa). For the globe and each region, the probability of persistent contrail formation (P_{form}) has been calculated from the potential fractional contrail coverage according to Burkhardt et al. (2008) and the probability of contrail formation. The probability of contrail formation close to the Schmidt-Appleman (SA)-threshold (P_{NTH}) has been obtained by

$$P_{NTH} = P_{form} \cdot \int_{0K}^{3K} PDF \cdot d\Delta T, \quad (A1)$$

with PDF indicating the probability density function of the temperature difference between ambient temperature and the SA-threshold temperature (ΔT) around the main cruise level (Figure 3a). Equation (A1) gives the fraction of contrails forming near the SA-threshold. Correcting for the temperature bias, T_{bias} , we determine the corrected probability of contrail formation ($P_{form,cor}$) and the corrected probability of contrail formation close to the SA-threshold ($P_{NTH,cor}$) as follows:

$$P_{form,cor} = P_{form} \cdot \frac{\int_{T_{bias}}^{25K} PDF \cdot d\Delta T}{\int_{0}^{25K} PDF \cdot d\Delta T}, \quad (A2)$$

$$P_{NTH,cor} = P_{form,cor} \cdot \frac{\int_{T_{bias}}^{T_{bias}+3K} PDF \cdot d\Delta T}{\int_{T_{bias}}^{25K} PDF \cdot d\Delta T}. \quad (A3)$$

Acknowledgments

The authors thank Simon Unterstrasser and three anonymous reviewers for their helpful comments on the manuscript of this paper and Lisa Bock for support with the model. The presented data are available online (<https://www.pa.op.dlr.de/opendata/JGR-201803AB>). This work was funded by the DLR project ECLIF (Emission and CLimate Impact of alternative Fuels). Computational resources were made available by the German Climate Computing Centre (DKRZ) through support from the German Federal Ministry of Education and Research.

References

- Anderson, B. E., Cofer, W. R., Bagwell, D. R., Barrick, J. W., Hudgins, C. H., & Brunke, K. E. (1998). Airborne observations of aircraft aerosol emissions 1: Total nonvolatile particle emission indices. *Geophysical Research Letters*, 25, 1689–1692.
- Beyersdorf, A. J., Timko, M. T., Ziemba, L. D., Bulzan, D., Corporan, E., Herndon, S. C., et al. (2014). Reductions in aircraft particulate emissions due to the use of Fischer-Tropsch fuels. *Atmospheric Chemistry and Physics*, 14(1), 11–23. <https://doi.org/10.5194/acp-14-11-2014>
- Bier, A., Burkhardt, U., & Bock, L. (2017). Synoptic control of contrail cirrus life cycles and their modification due to reduced soot number emissions. *Journal of Geophysical Research: Atmospheres*, 122, 11,584–11,603. <https://doi.org/10.1002/2017JD027011>
- Bock, L., & Burkhardt, U. (2016a). The temporal evolution of a long-lived contrail cirrus cluster: Simulations with a global climate model. *Journal of Geophysical Research: Atmospheres*, 121, 3548–3565. <https://doi.org/10.1002/2015JD024475>
- Bock, L., & Burkhardt, U. (2016b). Reassessing properties and radiative forcing of contrail cirrus using a global climate model. *Journal of Geophysical Research: Atmospheres*, 121, 9717–9736. <https://doi.org/10.1002/2016JD025112>
- Bond, T. C., Doherty, J., Fahey, D. W., Forster, P. M., Bernsten, T., De Angelo, B. J., et al. (2013). Bounding the role of black carbon in the climate system—A scientific assessment. *Journal of Geophysical Research: Atmospheres*, 118, 5380–5552. <https://doi.org/10.1002/jgrd.50171>
- Boucher, O., Randall, D., Artaxo, P., Bretherton, C., Feingold, G., Forster, P., et al. (2013). Clouds and aerosols. In T. Stocker, et al. (Eds.), *Climate change 2013: The physical science basis. Contribution of working group I to the Fifth Assessment Report of the Intergovernmental Panel on Climate Change* (Vol. 7, pp. 571–658). Cambridge, UK, and New York: Cambridge University Press.
- Burkhardt, U., Bock, L., & Bier, A. (2018). Mitigating the contrail cirrus climate impact by reducing aircraft soot number emissions. *npj Climate and Atmospheric Science*, 37, 1–7. <https://doi.org/10.1038/s41612-018-0046-4>
- Burkhardt, U., & Kärcher, B. (2009). Process-based simulation of contrail cirrus in a global climate model. *Journal of Geophysical Research*, 114, D16201. <https://doi.org/10.1029/2008JD011491>
- Burkhardt, U., & Kärcher, B. (2011). Global radiative forcing from contrail cirrus. *Nature Climate Change*, 1(1), 54–58. <https://doi.org/10.1038/NCLIMATE1068>
- Burkhardt, U., Kärcher, B., Ponater, M., Gierens, K., & Gettelman, A. (2008). Contrail cirrus supporting areas in model and observations. *Geophysical Research Letters*, 35, L16808. <https://doi.org/10.1029/2008GL034056>

- Chen, C.-C., & Gettelman, A. (2013). Simulated radiative forcing from contrails and contrail cirrus. *Atmospheric Chemistry and Physics*, 13, 12,525–12,536. <https://doi.org/10.5194/acp-13-12525-2013>
- Febvre, G., Gayet, J., Minikin, A., Schlager, H., Shcherbakov, V., Jourdan, O., et al. (2009). On optical and microphysical characteristics of contrails and cirrus. *Journal of Geophysical Research*, 114, D02204. <https://doi.org/10.1029/2008JD010184>
- Foust, M., Thomsen, D., Stickles, R., Cooper, C., & Dodds, W. (2011). Development of the GE Aviation Low Emissions TAPS Combustor for Next Generation Aircraft Engines, *AIAA Paper*.
- Gierens, K., & Vazquez-Navarro, M. (2018). Statistical analysis of contrail lifetimes from a satellite perspective. *Meteorologische Zeitschrift*, 183–193. <https://doi.org/10.1127/metz/2018/0888>
- Haywood, J. M., Allan, R. P., Bornemann, J., Forster, P. M., Francis, P. N., Milton, S., et al. (2009). A case study of the radiative forcing of persistent contrails evolving into contrail-induced cirrus. *Journal of Geophysical Research*, 114, D24201. <https://doi.org/10.1029/2009JD012650>
- Hertwig, E., von Storch, J.-S., Handorf, D., Dethloff, K., Fast, I., & Krismer, T. (2015). Effect of horizontal resolution on ECHAM6-AMIP performance. *Climate Dynamics*, 45, 185–211. <https://doi.org/10.1007/s00382-014-2396-x>
- Hoose, C., & Möhler, O. (2012). Heterogeneous ice nucleation on atmospheric aerosols: A review of results from laboratory experiments. *Atmospheric Chemistry and Physics*, 12, 9817–9854. <https://doi.org/10.5194/acp-12-9817-2012>
- International Civil Aviation Organization (2013). *Environmental Report 2013*, Chap. 1: Aviation and environment.
- International Organization for Standardization (1975). *Standard Atmosphere*. ISO 2533:1975.
- Kärcher, B., Burkhardt, U., Bier, A., Bock, L., & Ford, I. J. (2015). The microphysical pathway to contrail formation. *Journal of Geophysical Research: Atmospheres*, 120, 7893–7927. <https://doi.org/10.1002/2015JD023491>
- Kärcher, B., Möhler, O., DeMott, P. J., Pechtl, S., & Yu, F. (2007). Insights into the role of soot aerosols in cirrus cloud formation. *Atmospheric Chemistry and Physics*, 7, 4203–4227. www.atmos-chem-phys.net/7/4203/2007/
- Kärcher, B., & Yu, F. (2009). Role of aircraft soot emissions in contrail formation. *Geophysical Research Letters*, 36, L01804. <https://doi.org/10.1029/2008GL036649>
- Köhler, H. (1936). The nucleus in and the growth of hygroscopic droplets. *Transactions of the Faraday Society*, 32, 1152–1161.
- Koop, T., Luo, B. P., Tsias, A., & Peter, T. (2000). Water activity as the determinant for homogeneous ice nucleation in aqueous solutions. *Nature*, 406(6796), 611–614.
- Kurz, C. (2007). *Entwicklung und Anwendung eines gekoppelten Klima-Chemie-Modellsystems: Globale Spurengastransporte und chemische Umwandlungsprozesse*, Doctoral thesis, Ludwigs-Maximilians-Universität München, München, Germany, DLR Forschungsbericht 2007–12.
- Lamquin, N., Stubenrauch, C., Gierens, K., Burkhardt, U., & Smit, H. (2012). A global climatology for upper-tropospheric ice supersaturation occurrence inferred from the atmospheric infrared sounder calibrated by MOZAIC. *Atmospheric Chemistry and Physics*, 12(1), 381–405. <https://doi.org/10.5194/acp-12-381-2012>
- Lee, D., Fahey, D., Forster, P., Newton, P., Wit, R., Lim, L., Owen, B., et al. (2009). Aviation and global climate change in the 21st century. *Atmospheric Environment*, 43(22–23), 3520–3537. <https://doi.org/10.1016/j.atmosenv.2009.04.024>
- Lewellen, D., & Lewellen, W. (2001). The effects of aircraft wake dynamics on contrail development. *Journal of Atmospheric Science*, 58, 390–406.
- Lohmann, U., Spichtinger, P., Heidt, S., Peter, T., & Smit, H. (2008). Cirrus clouds and ice supersaturation regions in a global climate model. *Environmental Research Letters*, 3, 045022(4). <https://doi.org/10.1016/j.atmosenv.2009.04.024>
- Minikin, A., Petzold, A., Strom, J., Krejci, J. R., Seifert, M., van Velthoven, P., Schlager, H., et al. (2003). Aircraft observations of the upper tropospheric fine particle aerosol in the Northern and Southern Hemispheres at midlatitudes. *Geophysical Research Letters*, 30(10), 1503. <https://doi.org/10.1029/2002GL016458>
- Minnis, P., Young, D. F., Garber, D. P., Nguyen, L., Smith, W. L., & Palikonda, R. (1998). Transformation of contrails into cirrus during SUCCESS. *Geophysical Research Letters*, 25, 1157–1160.
- Moore, R. H., Shook, M., Beyersdorf, A., Corr, C., Herndon, S., Knighton, W. B., et al. (2015). Influence of jet fuel composition on aircraft engine emissions: A synthesis of aerosol emissions data from the NASA APEX, AAFEX and ACCESS missions. *Energy & Fuels*, 29(4), 2591–2600. <https://doi.org/10.1021/ef502618w>
- Moore, R. H., Thornhill, K. L., Weinzierl, B., Sauer, D., D'Ascoli, E., Kim, J., et al. (2017). Biofuel blending reduces particle emissions from aircraft engines at cruise conditions. *Nature*, 543(7645), 411–415. <https://doi.org/10.1038/nature21420>
- Newinger, C., & Burkhardt, U. (2012). Sensitivity of contrail cirrus radiative forcing to air traffic scheduling. *Journal of Geophysical Research*, 117, D10205. <https://doi.org/10.1029/2011JD016736>
- Paoli, R., & Shariff, K. (2016). Contrail modeling and simulation. *Annual Review of Fluid Mechanics*, 48, 393–427. <https://doi.org/10.1146/annurev-fluid-010814-013619>
- Petters, M. D., & Kreidenweis, S. M. (2007). A single parameter representation of hygroscopic growth and cloud condensation nucleus activity. *Atmospheric Chemistry and Physics*, 7, 1961–1971. www.atmos-chem-phys.net/7/1961/2007/
- Petzold, A., Döpelheuer, A., Brock, C. A., & Schröder, F. (1999). In situ observations and model calculations of black carbon emission by aircraft at cruise altitude. *Journal of Geophysical Research*, 104, 22,171–22,181.
- Petzold, A., Krämer, M., Neis, P., Rolf, C., Rohs, S., Berkes, F., et al. (2017). Upper tropospheric water vapour and its interaction with cirrus clouds as seen from IAGOS long-term routine in situ observations. *Faraday Discussions*, 200, 229–249. <https://doi.org/10.1039/c7fd00006e>
- Roeckner, E., Baeuml, G., Bonaventura, L., Brokopf, R., Esch, M., Giorgetta, M., et al. (2003). *The atmospheric general circulation model ECHAM5. Part 1: Model description*, Report (Vol. 349, p. 127). Hamburg, Germany: Max-Planck-Institut für Meteorologie.
- Roeckner, E., Brokopf, R., Esch, M., Giorgetta, M., Hagemann, S., Kornblüeh, L., et al. (2006). Sensitivity of simulated climate to horizontal and vertical resolution in the ECHAM5 atmosphere model. *Journal of Climate*, 19(16), 3771–3791.
- Schröder, F., Kärcher, B., Durore, C., Ström, J., Petzold, A., Gayet, J., et al. (2000). On the transition of contrails into cirrus clouds. *Journal of the Atmospheric Sciences*, 57(4), 464–480. [https://doi.org/10.1175/1520-0469\(2000\)057<0464:OTTOCI>2.0.CO;2](https://doi.org/10.1175/1520-0469(2000)057<0464:OTTOCI>2.0.CO;2)
- Schumann, U. (1996). On conditions for contrail formation from aircraft exhausts. *Meteorologische Zeitschrift*, 5, 4–23.
- Schumann, U., & Heymsfield, A. (2017). On the lifecycle of individual contrails and contrail cirrus. *Meteorological Monographs*, 58, 3.1–3.24. <https://doi.org/10.1175/AMSMONOGRAPHS-D-16-0005.1>
- Schumann, U., Penner, J. E., Chen, Y., Zhou, C., & Graf, K. (2015). Dehydration effects from contrails in a coupled contrail-climate model. *Atmospheric Chemistry and Physics*, 15(19), 11,179–11,199. <https://doi.org/10.5194/acp-15-11179-2015>
- Speth, R. L., Rojo, C., Malina, R., & Barrett, S. R. H. (2015). *Black carbon emissions reductions from combustion of alternative jet fuels* (Vol. 105, pp. 37–42). Cambridge, MA: Massachusetts Institute of Technology. <https://doi.org/10.1016/j.atmosenv.2015.01.040>

- Stier, P., Feichter, J., Kinne, S., Kloster, S., Vignati, E., Wilson, J., et al. (2005). The aerosol-climate model ECHAM5-HAM. *Atmospheric Chemistry and Physics*, 5(4), 1125–1156. <https://doi.org/10.5194/acp-5-1125-2005>
- Sundqvist, H. (1978). A parameterization scheme for non-convective condensation including prediction of cloud water content. *Quarterly Journal of the Royal Meteorological Society*, 104(441), 677–690.
- Sussmann, R., & Gierens, K. (1999). Lidar and numerical studies on the different evolution of vortex pair and secondary wake in young contrails. *Journal of Geophysical Research*, 104, 2131–2142.
- Unterstrasser, S. (2016). Properties of young contrails—A parametrisation based on large-eddy simulations. *Atmospheric Chemistry and Physics*, 16(4), 2059–2082. <https://doi.org/10.5194/acp-16-2059-2016>
- Voigt, C., Schumann, U., Jurkat, T., Schäuble, D., Schlager, H., Petzold, A., et al. (2010). In-situ observations of young contrails—Overview and selected results from the CONCERT campaign. *Atmospheric Chemistry and Physics*, 10(18), 9039–9056. <https://doi.org/10.5194/acp-10-9039-2010>
- Wilkerson, J. T., Jacobson, M. Z., Malwitz, A., Balasubramanian, S., Wayson, R., Fleming, G., et al. (2010). Analysis of emission data from global commercial aviation: 2004 and 2006. *Atmospheric Chemistry and Physics*, 10(13), 6391–6408. <https://doi.org/10.5194/acp-10-6391-2010>